Bimetallic Fe x Pt 100– x Nanoparticles Immobilized on Supported Ionic Liquid Phases as Hydrogenation and Hydrodeoxygenation Catalysts: Influence of the Metal Content on Activity and Selectivity

Nataliia Marchenko, Lise-Marie Lacroix, Nicolas Ratel-Ramond, Walter Leitner, Alexis Bordet, Simon Tricard

Bimetallic Fe_xPt_{100-x} Nanoparticles Immobilized on Supported Ionic Liquid Phases as Hydrogenation and Hydrodeoxygenation Catalysts: Influence of the Metal Content on Activity and Selectivity

Nataliia Marchenko,[a] Lise-Marie Lacroix,[a,b] Nicolas Ratel-Ramond,[a] Walter Leitner, [c,d] Alexis Bordet,[c]* Simon Tricard [a]*

[a] *LPCNO, INSA, CNRS, Université de Toulouse, 135 avenue de Rangueil, 31077 Toulouse, France*

[b] *Institut Universitaire de France (IUF), 103 boulevard Saint Michel, 75005 Paris, France*

[c] *Max Planck Institute for Chemical Energy Conversion, Stiftstraße 34-36, 45470 Mülheim an der Ruhr, Germany*

[d] *Institut für Technische und Makromolekulare Chemie, RWTH Aachen University, Worringerweg 2, Aachen 52074, Germany*

[*] *Corresponding authors: tricard@insa-toulouse.fr, alexis.bordet@cec.mpg.de*

ABSTRACT

Iron-platinum nanoparticles of tunable Fe:Pt ratios were immobilized on an imidazolium-based supported ionic liquid phase (SILP). The resulting Fe_xPt_{100-x}@SILP materials were characterized and applied in catalysis. Electron microscopy confirmed the formation of small, well-dispersed, bimetallic nanoparticles in all the investigated materials. Magnetometry measurements evidenced a clear influence of the Fe:Pt ratio on the oxidation state of Fe in Fe_xPt_{100-x}@SILP. In particular, Fe appeared in the metallic state at x≤40, whereas partial oxidation was observed at x≥60. The catalytic properties of Fe_xPt_{100-x}@SILP materials were probed using the hydrogenation and hydrodeoxygenation of benzylic ketones as a model reaction. The Fe:Pt ratio of the nanoparticles was found to have a critical influence on the observed activity and selectivity, with clear synergistic effects. In particular, by diluting Pt with Fe sites, the ability of Fe_xPt_{100-x}@SILP catalysts to hydrogenate 6-membered aromatic rings was shut down for x≥40, while C=O hydrogenation activity was preserved. In addition, $Fe_{40}Pt_{60}$@SILP showed excellent hydrodeoxygenation activity and selectivity with acetophenone derivatives in the absence of acid additives. This remarkable reactivity, out of reach for monometallic Pt@SILP, is attributed to the enhanced oxophilicity of Fe in FePt catalysts favoring C=O activation and cleavage.

KEYWORDS

bimetallic nanoparticles, supported ionic liquid phases, platinum, iron, hydrogenation, hydrodeoxygenation, catalysis, magnetism

INTRODUCTION

Most of the industrial hydrogenation processes are conducted in the presence of heterogeneous catalysts. Noble metal catalysts such as Adams catalyst[1] or palladium black[2] are in use for more than

100 years due to their high activity and reusability. However, improvements in terms of selectivity and functional groups tolerance require continuous advancement in catalyst design for different fields of chemistry, as *e.g.* fine chemicals synthesis, pharmaceutical or agrochemical industry. In addition, the diversification of carbon feedstock associated to the rise of renewable resources represents a challenge, making the development of new catalytic systems of crucial importance.[3] Different strategies were developed to tune the selectivity of heterogeneous catalysts by modification of electronic or/and steric properties of the active surface.[4] Particularly, the design of bimetallic nanoparticles (NPs) has attracted tremendous attention since synergetic interactions between different metals showed to unlock selectivities that cannot be reached with monometallic catalysts.[5–9] For example, the alloying of noble metals with 3d metals provided selectivity control in the hydrogenation or hydrodeoxygenation (HDO) of various functionalities including alkynes, aldehydes and ketones, carboxylic acids, nitroaromatics, amides, etc.[10–19] In this context, the controlled preparation of well-defined nanoparticles varying systematically the composition of the two distinct metal components is of great importance. Based on an organometallic approach for the assembly of nanoparticles on molecularly modified surfaces,[20] our groups reported recently the versatile synthesis of Fe_xRu_{100-x}, Co_xRu_{100-x}, and Co_xRh_{100-x} NPs on supported ionic liquid phases supports (SILPs). The application of these $M1_xM2_{100-x}$@SILP materials in catalysis evidenced the remarkable influence of the nature of the "diluting" 3d metal M1 and its relative ratio to the noble metal M2 on the overall hydrogenation performance.[21–23] In particular, synergistic effects were observed for the hydrogenation of aromatic ketones, with an enhancement of C=O hydrogenation activity for bimetallic NPs, while aromatic ring hydrogenation was completely shut down for specific metal ratios.

In order to further explore the potential of bimetallic NPs, we set our goal to systematically investigate NPs composed of Fe and Pt of defined compositions. Fe_xPt_{100-x} NPs have been widely studied in the past decade, in particular for their excellent magnetic properties.[24–26] In catalysis, Fe_xPt_{100-x} NPs have been mainly explored for the selective hydrogenation of conjugated aldehydes.[27–29] For example, Bai and co-workers synthesized and characterized Pt-based nanowires, which they applied to the hydrogenation of cinnamaldehyde.[30] While monometallic Pt catalysts hydrogenated both C=C and C=O double bonds to produce 3-phenyl-propanol, bimetallic FePt materials hydrogenated only the aldehyde functionality, leaving the C=C untouched. Applications in oxygen reduction reaction,[31,32] hydrogenation of unsaturated hydrocarbons[33] and nitroaromatics[34,35] were also punctually reported. However, to the best of our knowledge, systematic investigations of the reactivity of supported Fe_xPt_{100-x} NPs of tunable composition for the reduction of ketones are missing. They are nevertheless highly desirable, since the known enhanced electrophilic properties of Fe in Fe_xPt_{100-x} alloys[36,37] may provide access to reactivities that are out of reach for previously reported [noble metal-3d metal] bimetallic alloys.

Herein, we present the synthesis, characterization, and application of bimetallic Fe_xPt_{100-x} NPs of finely tunable Fe:Pt ratio immobilized on an imidazolium-based SILP support. The resulting Fe_xPt_{100-x}@SILP materials were characterized using a variety of techniques including electron microscopy (TEM, SEM-EDX), wide-angle X-Ray scattering (WAXS), infrared spectroscopy (IR), and vibrating-sample magnetometry (VSM). In particular, studying the magnetic properties of Fe_xPt_{100-x} NPs by VSM proved to be a simple and powerful approach to collect information about the oxidation state of Fe. Fe_xPt_{100-x}@SILP materials were applied to the reduction of aromatic ketones, a transformation of great importance not only for the fine chemical and pharmaceutical industries, but also for the conversion of biomass feedstock to value-added chemicals.[38] The influence of the Fe:Pt metal ratio on activity and selectivity was explored in a systematic manner, evidencing strong synergistic effects.

RESULTS AND DISCUSSION

1 Synthesis of the Fe_xPt_{100-x}@SILP materials

An imidazolium-based SILP was used as a support for its proven ability to facilitate the formation and stabilization of mono- and bimetallic nanoparticles.[22,23,39,40] The SILP support used in the present study was previously characterized by thermogravimetric analysis, and found thermally stable up to 350 °C.[39] It is chemically stable in most organic solvents, and can be used both under batch and continuous flow conditions. Preparation of the support was performed following a previously published procedure.[39] Briefly, the silane-functionalized IL [1-butyl-3-(3-triethoxysilylpropyl)imidazolium]NTf_2 (NTf_2 = bis(trifluoromethane)sulfonimide) was chemisorbed on dehydroxylated SiO_2 by silanization with a loading of 0.7 mmol.g^{-1}. The synthesis of bimetallic Fe_xPt_{100-x} NPs (with x = 100, 80, 60, 50, 40 20, 0) was achieved by adapting an organometallic approach developed by our groups for bimetallic FeRu, CoRu, and CoRh@SILP.[21–23] This approach involved the decomposition of the metal precursors $\{Fe[N(Si(CH_3)_3)_2]_2\}_2$ and $[Pt_2(dba)_3]$ (dba = dibenzylideneacetone) *in situ* in the presence of the SILP material under H_2 (3 bar) at 150 °C for 18 h with a mixture of anisole and THF as a solvent, to ensure a good solubility of both precursors (total metal loading = 0.35 mmol.g^{-1}) (Figure 1). $\{Fe[N(Si(CH_3)_3)_2]_2\}_2$ and $[Pt_2(dba)_3]$ were used since they possess similar decomposition rates. Using $[Pt(nbe)_3]$ or $[Pt(Me)_2(cod)]$ (nbe = norbornene, cod = 1,5-cyclooctadiene) resulted in large agglomerates (Figure S1). This synthetic approach provided access to a wide range of bimetallic Fe_xPt_{100-x}@SILP catalysts in which the Fe:Pt ratio was finely tuned by adjusting the relative amounts of precursors. To evaluate the influence of the SILP on the NP formation and catalytic properties, Fe_xPt_{100-x} NPs were also immobilized on unmodified silica (Fe_xPt_{100-x}@SiO_2) following the same procedure to act as reference materials.

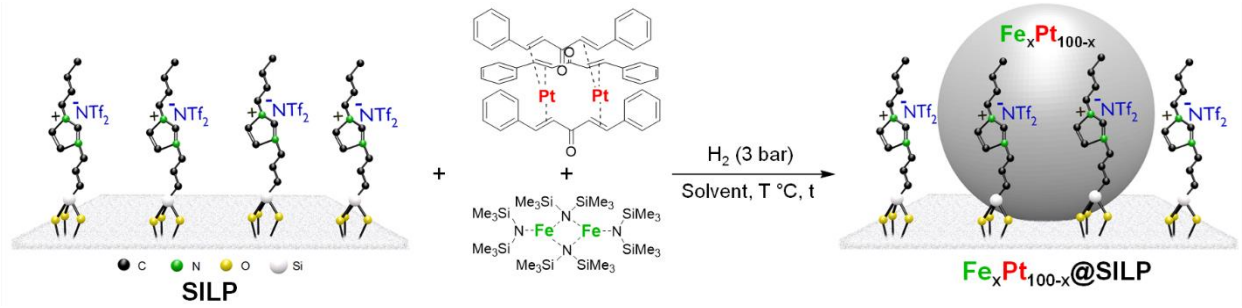

Figure 1. Illustration of our synthetic approach to Fe_xPt_{100-x}@SILP materials.

2 Characterization of the Fe_xPt_{100-x}@SILP materials

Characterization of the Fe_xPt_{100-x}@SILP materials by transmission electron microscopy (TEM) evidenced the formation of small NPs (1.5 – 2.5 nm) on the SILP for all the Fe:Pt ratios (Figure 2a, Figures S2 and S3). Pair distribution functions obtained by WAXS confirmed the face centered cubic structure for the NPs rich in platinum with correlation distances similar to the sizes obtained by TEM, thus proving the monocrystallinity of the nanoobjects (~2.5 nm for pure Pt and ~2.0 nm for $Fe_{40}Pt_{60}$ – Figure S4). On the contrary, for the $Fe_{80}Pt_{20}$@SILP samples, rich in iron, only the Pt-Pt distance and its harmonics could be observed on correlation distances smaller than 1 nm. This finding indicates that the objects were significantly less crystalized, suggesting some amorphization due to a large amount of Fe. High resolution imaging using HAADF-STEM and elemental mapping using STEM-EDX confirmed the bimetallic nature of Fe_xPt_{100-x} NPs, as exemplified for $Fe_{40}Pt_{60}$@SILP (Figure 2 and Figure S5; STEM = scanning transmission electron microscopy; HAADF = high angle annular dark field; EDX = energy-dispersive X-ray spectroscopy). Total metal loadings and ratios of metals were determined by SEM-EDX (SEM = scanning electron microscopy). The results are summarized in Table S1 and agree with theoretical values. TEM of $Fe_{40}Pt_{60}$@SiO_2 nanomaterials showed the formation of well-dispersed NPs

of 1.9 nm (Figure S3d). SEM-EDX evidenced only slight deviations from the theoretical loading and metal ratio, similar to the results obtained for Fe_xPt_{100-x}@SILP systems (Table S1).

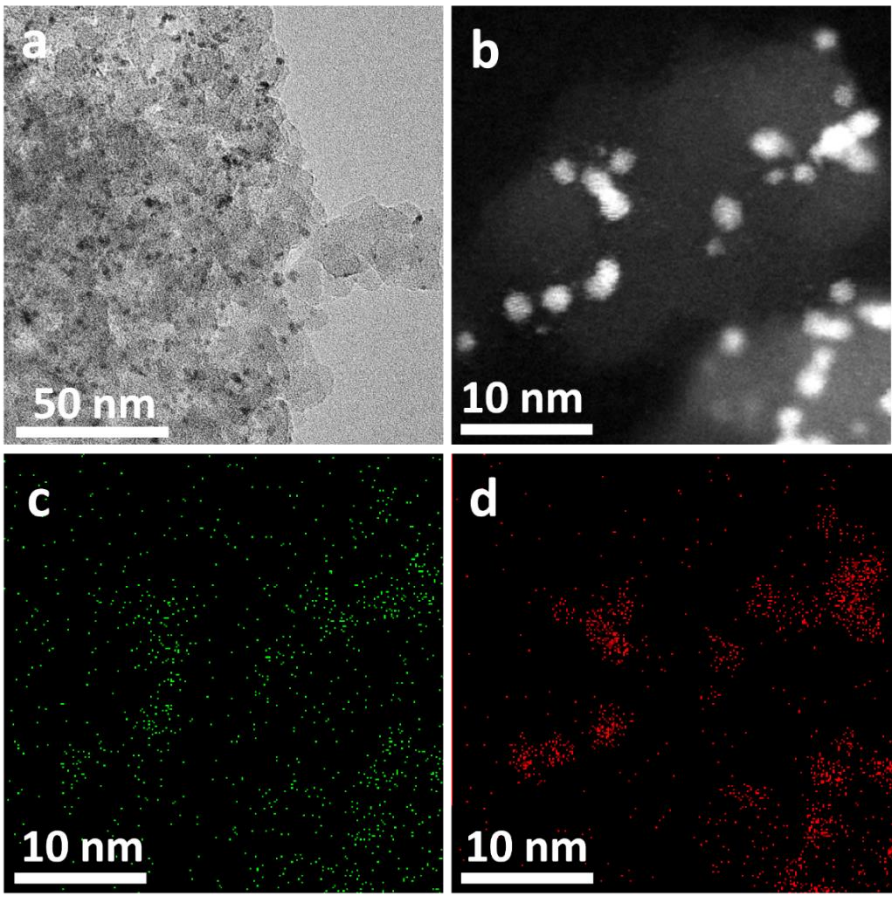

Figure 2. Characterization of Fe_xPt_{100-x}@SILP by electron microscopy, illustrated for $Fe_{40}Pt_{60}$@SILP. a) TEM (d = 2.0±0.4 nm); b) STEM-HAADF; c) STEM-HAADF-EDX elemental mapping of Fe-K; d) STEM-HAADF-EDX elemental mapping of Pt-L.

CO adsorption studies with FT-IR in transmission mode were performed for Fe_xPt_{100-x}@SILP materials (Figure S6), since this technique allows to investigate the alterations in electronic density on the surface of metal NPs. Fe_xPt_{100-x}@SILP powders were exposed to a CO atmosphere (3 bar) overnight, followed by CO gas removal under vacuum and analysis of the samples by FT-IR in a glovebox. For all samples, a vibration band of adsorbed CO was found in the 2018-2049 cm^{-1} range, which is characteristic of a linear adsorption mode of the CO molecule on Pt (Figure 3).[41,42] The vibrations of bridged CO that are usually present at the region of 1800-1900 cm^{-1} are hindered by the overtone of Si-O in the framework of the silica support (Figure S6).[43] While the CO vibration band was observed at 2049 cm^{-1} on Pt_{100}@SILP, a red shift was systematically observed on bimetallic Fe_xPt_{100-x}@SILP materials ($Fe_{20}Pt_{80}$: 2037 cm^{-1}; for $Fe_{40}Pt_{60}$: 2018 cm^{-1}; $Fe_{60}Pt_{40}$: 2034 cm^{-1}, $Fe_{80}Pt_{20}$: 2043 cm^{-1}). These results suggest that Fe can donate electronic density to more electronegative Pt, in agreement with observations made by other groups.[44,45] Interestingly, the red shift does not follow a linear trend as a function of the Fe content. This tendency may be explained by a change of the oxidation state of iron as a function of the Fe:Pt ratio. In a previous study on Fe_xRu_{100-x}@SILP materials, X-Ray absorption spectroscopy (XAS) evidenced the presence of metallic iron in the iron-poor alloys, but mainly oxidized iron in iron-rich alloys (Fe content > 50%).[21] Since oxidized iron species are electrophilic and can withdraw electron density, an increase in the amount of oxidized iron may be a reason for the smaller red shift observed with $Fe_{60}Pt_{40}$@SILP and $Fe_{80}Pt_{20}$@SILP as compared to $Fe_{40}Pt_{60}$@SILP.

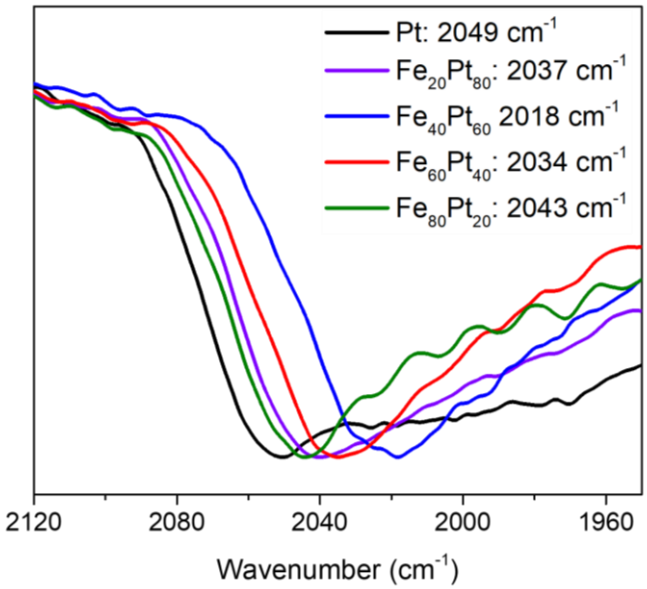

Figure 3. Transmission IR spectra of Fe_xPt_{100-x}@SILP after CO exposure – zoom on the terminal CO absorption band.

While catalysts are often studied by synchrotron-based XAS to determine their oxidation state, magnetometry, which is a fairly accessible technique, can be successfully used for magnetic materials such as Fe-, Co-, or Ni-containing systems. Indeed, the evolution of the magnetization M *vs* the applied magnetic field H, combined with the temperature dependence of the low field magnetization M *vs* T, allow distinguishing between a ferromagnetic state, expected for some of the purely metallic materials, and an antiferromagnetic/ferrimagnetic state, observed for oxidized materials. M *vs* H curves of Fe_xPt_{100-x}@SILP with x = 40, 60, 80 are presented and compared with pure Fe@SILP on Figure 4a. For every catalyst, the 5 K magnetization curve does not saturate at high field but exhibit a linear contribution, typical for paramagnetic species. Such behavior is commonly observed for small nanoparticles[46] and arises from the large proportion of surface atoms which, depending on the nature of the ligands and their coordination mode, can exhibit paramagnetic properties. The paramagnetic contribution is fairly similar for all the catalysts, in agreement with the same mean diameter of the NPs determined by TEM. To further analyze the core properties, the paramagnetic contribution was subtracted as shown in Figure S7a and the resulting hysteresis loops were compared (Figure S8a). The spontaneous magnetization (M_{spont}) defined as the maximum magnetization after paramagnetic subtraction, was determined for each sample. Interestingly, the M_{spont} values were fairly similar for $Fe_{40}Pt_{60}$@SILP and $Fe_{60}Pt_{40}$@SILP but diminished significantly for larger Fe content, the lower value being obtained for pure Fe NPs (Table 1). Since Fe(0) atoms have a larger magnetic moment than Pt(0) atoms,[47] one would have expected an opposite trend for purely metallic nanoparticles. However, this trend is consistent with a partial oxidation of the iron-rich nanoparticles, which was further confirmed by the analysis of the coercive field. Positive and negative coercive fields (H_c^+ and H_c^-) correspond to the field at which the magnetization is null (Figure S7b). They are symmetrical for Fe_xPt_{100-x}@SILP NPs for x = 40 and 60 with slightly smaller values of H_c for $Fe_{60}Pt_{40}$@SILP (Figure S8b and Table 1). However, the hysteresis cycle is shifted towards the negative value for x = 80 and 100, as characterized by the exchange bias field $H_{ex} = \frac{H_C^+ + H_C^-}{2}$ (Table 1). The appearance of such a bias is characteristic of the presence of an oxide shell on the NPs.[46] To further confirm this conclusion, the $Fe_{40}Pt_{60}$@SILP NPs were deliberately exposed to air for 7 days (Figure 4b). As expected, the spontaneous magnetization was reduced by 75%, the coercive field decreased by 40% and an exchange bias field appeared.

Additionally, the temperature evolution of the magnetization was investigated following the classical zero field cooling / field cooling experiments (ZFC/FC). At first, the samples were cooled down from 300 K to 5 K in the absence (resp. in presence) of external magnetic field. The so-called ZFC (resp. FC) magnetization was recorded during the warming up from 5 K to 300 K while applying a modest field of $\mu_0 H$ = 10 mT. ZFC/FC plots recorded for Fe_xPt_{100-x}@SILP samples display the usual signatures observed in magnetic nanoparticle systems (Figure S9). The curves overlap at high temperatures and exhibit a paramagnetic-like decay with increasing temperature, indicating the superparamagnetic behavior of the particles. The ZFC curve recorded for $Fe_{40}Pt_{60}$@SILP and $Fe_{60}Pt_{40}$@SILP follows a typical behavior of ferromagnetic NPs, namely a clear maximum on the ZFC curve, corresponding to the blocking temperature T_b, which indicates the temperature of the transition from the "frozen" ferromagnetic state to the superparamagnetic state. From 5 K to T_b the magnetization exhibits a monotonal increase. On the contrary, the ZFC curves recorded for $Fe_{80}Pt_{20}$@SILP, Fe@SILP and oxidized $Fe_{40}Pt_{60}$@SILP NPs showed a decrease at very low temperature, before increasing again up to T_b (Figure 4c). Such a behavior at low temperature is a signature of antiferromagnetic states due to the presence of oxides, thus again confirming that the particles are partially oxidized for an iron content higher than 60%.

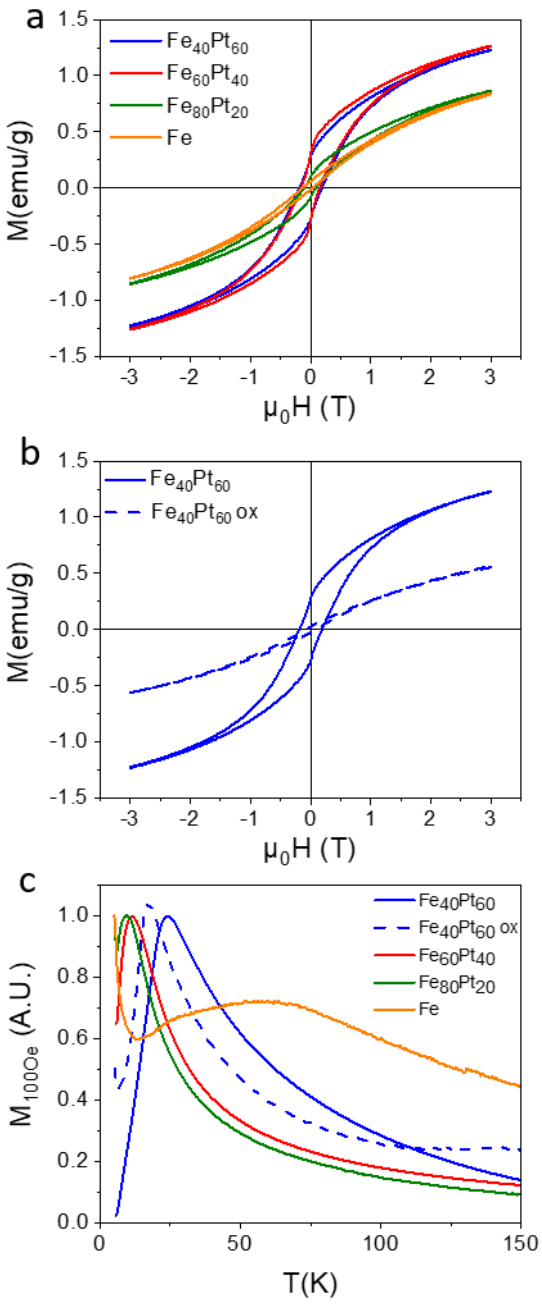

Figure 4. a) Hysteresis cycle (M *vs* H curve) recorded between +/- 3 T at 5 K for the different catalyst Fe_xPt_{100-x}@SILP; b) 3 T hysteresis cycle recorded at 5 K for $Fe_{40}Pt_{60}$@SILP catalyst as prepared (blue line) and after 7 days of air exposure (dash line); c) M *vs* T curve recorded at μ_0H = 10 mT after zero-field cooling procedure.

Table 1. Coercive field, exchange bias field, and saturation magnetization values for different Fe_xPt_{100-x}@SILP materials.

Sample	μ_0H_c, mT	μ_0H_{ex}, mT	M_{spont}, emu/g
$Fe_{40}Pt_{60}$@SILP	220	-	0.77
$Fe_{40}Pt_{60}$@SILP (oxidized)	130	-5	0.20
$Fe_{60}Pt_{40}$@SILP	180	-	0.82
$Fe_{80}Pt_{20}$@SILP	115	-15	0.44
Fe	125	-75	0.36

H_C: coercive field, H_{ex}: exchange bias field; M_{spont} corresponds to the spontaneous magnetization, calculated after the removal of the paramagnetic contribution.

3 Catalysis

The catalytic performance of the Fe_xPt_{100-x}@SILP materials was studied using the hydrogenation of acetophenone (**1**) as a model reaction (Figure 5a). Selective reduction of aromatic ketones is a synthetically important transformation since the formed secondary alcohols are used as versatile building blocks and as target compounds in fragrances and flavors.[48,49] In a more general context, reduction of ketones is an important transformation for biomass valorization.[16,50,51] Substrate **1** possesses an aromatic ring and a benzylic ketone, giving the opportunity to probe the reactivity of Fe_xPt_{100-x}@SILP catalysts for different prototypical functional groups. The hydrogenation of **1** can proceed through two different pathways, with either 1-phenylethanol (**1a**) or 1-cyclohexylethan-1-one (**1b**) as intermediates before reaching the fully saturated product 1-cyclohexylethanol (**1c**). Eventually, HDO of **1a** and **1c** can also be observed, typically using multifunctional catalytic systems possessing acidic functionalities.[50,52,53] Figure 5b shows conversions and product yields as a function of the Pt content in Fe_xPt_{100-x} NPs, where all the reactions were performed under identical conditions (T = 175 °C, p(H_2) = 50 bar, t = 16 h, solvent - heptane). Monometallic Fe@SILP did not show any activity under these conditions, consistent with previous observations.[22] Increasing the Pt content in $Fe_{80}Pt_{20}$@SILP resulted in 34% conversion with **1a** (30%) as a major product. Full conversion was reached using $Fe_{60}Pt_{40}$@SILP, still with **1a** (56%) as a main product. Interestingly, a large amount of ethylbenzene (**1d**, 44%) was observed as well, indicating a promising hydrodeoxygenation activity of Fe_xPt_{100-x}@SILP catalysts. The yield of **1d** was substantially higher using $Fe_{40}Pt_{60}$@SILP, reaching 83% with only traces of aromatic ring hydrogenation. Remarkably, such hydrodeoxygenation activity of unsubstituted acetophenone was not observed with other bimetallic NPs immobilized on the same SILP.[21–23] Further increasing the Pt content led to a switch in the product distribution, with the formation of **1c** as the major product with $Fe_{20}Pt_{80}$@SILP and Pt_{100}@SILP (53% and 97%, respectively). Strikingly, only traces of hydrodeoxygenated product with saturated ring (ethylcyclohexane **1e**) could be observed when using Pt_{100}@SILP. Based on this result we assume that 80% of Pt led to the formation of Pt atom ensembles that were big enough to enable planar adsorption and hydrogenation of the aromatic ring.[54] The same catalytic test was also performed with the reference $Fe_{40}Pt_{60}$@SiO_2. In this case, together with 43% of the product **1d**, a large amount of products with saturated ring **1c** (14%) and **1e** (43%) was formed. Since Pt ensembles are responsible for ring hydrogenation as it was observed for $Fe_{20}Pt_{80}$@SILP and Pt_{100}@SILP, this result indicated that it might be difficult to achieve a controlled formation of bimetallic $Fe_{40}Pt_{60}$ NPs on unmodified silica support, in agreement with previous observations.[22,23,40]

HDO of acetophenones typically requires the presence of an acid additive,[52,53,55–59] activating substituents,[40,60] or high temperatures.[61] For example, using similar reaction conditions (50 bar H_2, 175°C, 16 h), an acidic $Fe_{25}Ru_{75}$@SILP-SO_3H catalyst was required to produce 91% of **1d** from **1**.[53] Meanwhile, the use of $Fe_{25}Ru_{75}$@SILP without acidic sites resulted only in 21% of **1d**.[60] In FePt bimetallics, Fe species are known to possess a Lewis acidic character, allowing them to act as adsorption sites and activate CO or NO_2 groups for example.[62,63] Therefore, we attribute the observed HDO activity to the presence of oxophilic iron sites in the Fe_xPt_{100-x} serving as weak Lewis acids and assisting selective activation and cleavage of aromatic C=O. This hypothesis is supported by several studies showing that incorporation of oxophilic 3d metals (in particular Fe or Co) in Pt or Pd NPs facilitates C-O adsorption and cleavage promoting the HDO of furfural derivatives.[17,18,37,64] For example, Luo and co-workers reported the selective hydrodeoxygenation of 5-hydroxymethylfurfural to dimethylfuran using Pt_3Co_2 NPs composed of a Pt-rich core and a Co_2O_3 surface.[17] The authors showed through DFT studies the importance of this cobalt oxide surface to promote HDO activity.

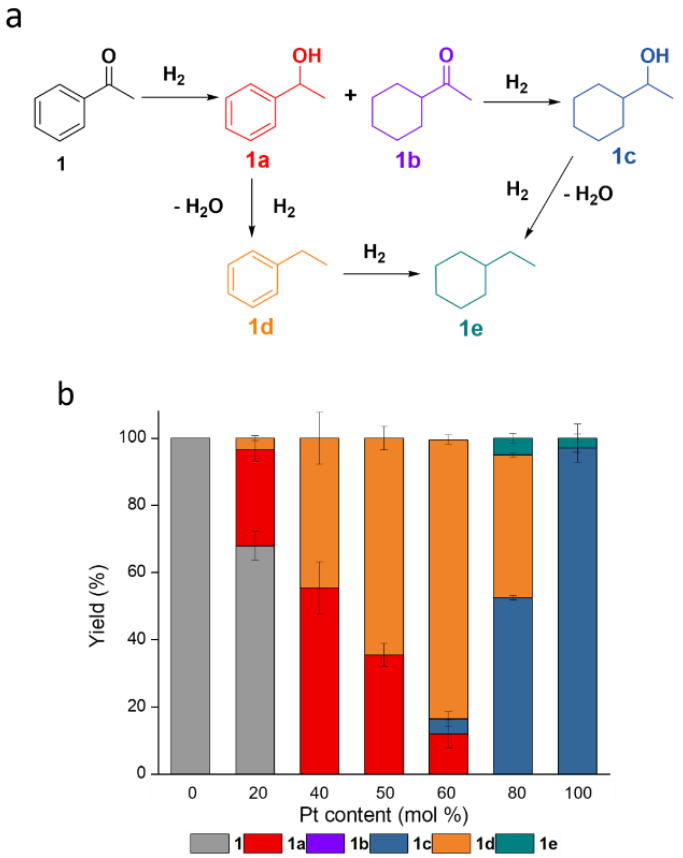

Figure 5. a) Reaction pathways for the reduction of acetophenone; b) reduction of acetophenone using a series of Fe_xPt_{100-x}@SILP catalysts with different Fe:Pt ratios. Reaction conditions: Catalyst (0.005 mmol metal), **1** (0.125 mmol, 25 eq.), heptane (0.5 mL), H_2 (50 bar), 175 °C, 16 h. Yields were determined by GC-FID using tetradecane as an internal standard. Data points are average values of a minimum of two experiments and error bars represent standard deviations.

To gain additional insight into the reactivity of the catalysts, time profiles of product formation were recorded using $Fe_{40}Pt_{60}$@SILP and $Fe_{20}Pt_{80}$@SILP (Figure 6). With $Fe_{40}Pt_{60}$@SILP, full conversion was observed after 1 h, with a product mixture composed of **1a** (55%), **1d** (43%, initial rate = 18 $mmol.L^{-1}.mmol_{Pt}^{-1}$), and traces of **1c** (2%). With increasing reaction time, **1a** was progressively converted into **1d**, giving the hydrodeoxygenated aromatic product **1d** in excellent yield and selectivity (95%) after 24 h. In this case, the hydrogenation clearly proceeded through the hydrogenation of the carbonyl moiety, while aromatic ring hydrogenation was shut down. Using $Fe_{20}Pt_{80}$@SILP, a mixture of **1a** (22%), **1c** (50%), and **1d** (28%, initial rate = 8.5 $mmol.L^{-1}.mmol_{Pt}^{-1}$) was observed after 1 h, indicating that the reaction also proceeded through the intermediate **1a**, and that this catalyst is active for aromatic ring hydrogenation. Interestingly, extending the reaction time to 4 h led to a mixture of **1c** (52%) and **1d** (40%) that was not significantly further converted even after 16 h (52% and 42%, respectively). While the very slow hydrodeoxygenation of **1c** to **1e** can be related to the difficulty to form a stable carbocation intermediate form **1c**, the fact that **1d** was barely further hydrogenated to **1e** (4%) is more surprising, as $Fe_{20}Pt_{80}$@SILP clearly possesses aromatic ring hydrogenation activity. Thus, the hydrogenation of ethylbenzene (**1d**) was investigated with this catalyst under standard reaction conditions. Strikingly, only 2% conversion to ethylcyclohexane (**1e**) was observed with $Fe_{20}Pt_{80}$@SILP after 16 h (Table S2), supporting the results of the time profile. In contrast, full conversion was achieved with the monometallic catalyst Pt@SILP, and with $Fe_{40}Pt_{60}$@SiO_2. To identify the reaction intermediates formed when using the monometallic Pt@SILP catalyst, 2 h reactions were conducted with a larger substrate: catalyst ratio (1500 eq. of **1** with respect to Pt – Table S3). At 79% of conversion, both the unsaturated alcohol **1a** (52%) and the saturated ketone **1b** (13%) were observed, indicating

that both hydrogenation pathways occur simultaneously with Pt@SILP. However, **1a** being the major intermediate suggests that C=O hydrogenation proceeds faster than aromatic ring hydrogenation. Interestingly, for bimetallic Fe_xPt_{100-x}@SILP catalysts, the formation of intermediate **1b** was never observed, indicating a decrease in the rate of the aromatic ring hydrogenation upon addition of Fe. A similar behavior was previously observed with other bimetallic catalysts (*e.g.* FeRu, CoRu, CoRh),[21–23] and can be attributed to the absence of ensembles of 3-4 adjacent noble metal atoms required to hydrogenate 6-membered aromatic rings.[22,23]

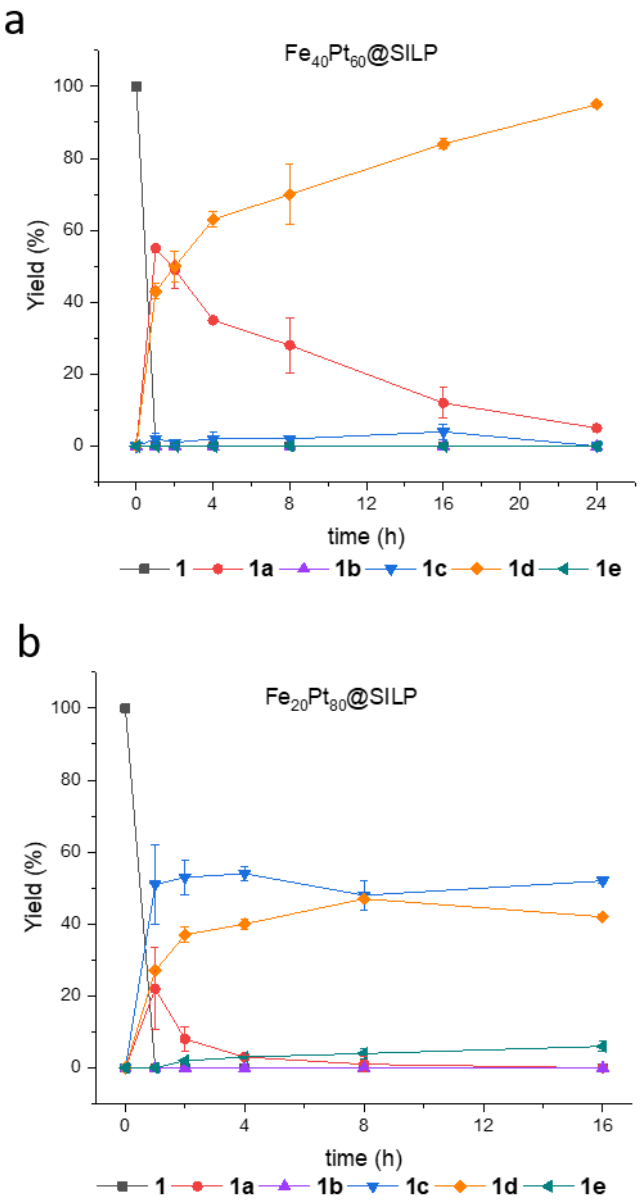

Figure 6. Time profiles of acetophenone hydrogenation recorded using a) $Fe_{40}Pt_{60}$@SILP, b) $Fe_{20}Pt_{80}$@SILP. Reaction conditions: Catalyst (0.005 mmol metal), **1** (0.125 mmol, 25 eq.), heptane (0.5 mL), H_2 (50 bar), 175°C. Yields were determined by GC-FID using tetradecane as an internal standard. Data points are average values of a minimum of two experiments and error bars represent standard deviations.

To explore the versatility of the $Fe_{40}Pt_{60}$@SILP catalyst in hydrodeoxygenation reactions, para-substituted acetophenone derivatives were selected for a reaction scope and tested under standard conditions (50 bar of H_2, 175°C, 16 h). The results are summarized in Table 2. High yields (70% - 99%) of the aromatic alkane products were obtained in all cases, without any aromatic ring hydrogenation.

Hydrodeoxygenation appeared to be facilitated by the presence of electron-donating substituents on the aromatic ring, while electron-withdrawing group such as CF_3 slowed down the reaction, in agreement with previous observations.[61]

Table 2. Selective hydrogenation of acetophenone derivatives using $Fe_{40}Pt_{60}$@SILP.

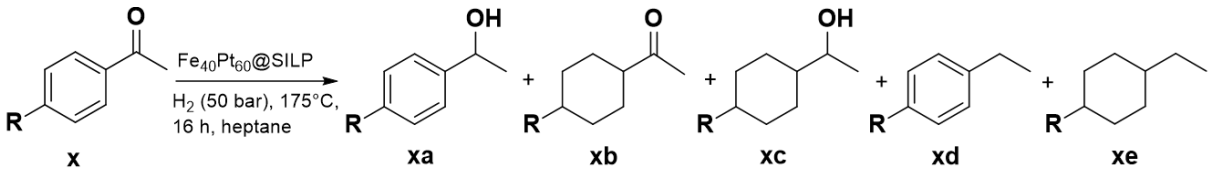

x	R	X (%)	Y **xa** (%)	Y **xb** (%)	Y **xc** (%)	Y **xd** (%)	Y **xe** (%)
1	H	>99	12	0	4	84	0
2	OCH_3	>99	0	0	0	>99	0
3	CH_3	>99	0	0	0	>99	0
4[a]	Cl	>99	0	0	0	96	0
5[a]	F	>99	1	0	0	97	0
6	CF_3	>99	30	0	0	70	0

Reaction conditions: Catalyst (13.6 mg, 0.005 mmol metal), substrate (0.125 mmol, 25 eq.), heptane (0.5 mL), H_2 (50 bar), 175°C, 16 h. Conversion and yield were determined by GC-FID using tetradecane as internal standard. Data points are average value of minimum two experiments. X = conversion, Y= yield. [a] side product is **1d**.

CONCLUSIONS

In conclusion, new Fe_xPt_{100-x}@SILP materials with tunable ratios of Fe:Pt were synthesized and fully characterized with a combination of electron microscopy techniques, structural analysis by WAXS, FTIR spectroscopy, and magnetometry. Magnetometry is an uncommon tool to characterize catalytic materials, nevertheless it proved to be highly efficient in characterizing the oxidation degree of our magnetic catalyst, and act as a widely accessible alternative to XAS in synchrotron facilities. Catalytic performances of Fe_xPt_{100-x}@SILP materials were probed for the hydrogenation and hydrodeoxygenation of acetophenone derivatives. Both activity and selectivity were found to be highly sensitive to the Fe:Pt ratio. Monometallic Pt@SILP gave saturated alcohols, whereas having 40% Fe in the catalyst resulted in HDO of the ketone, while preserving aromaticity of the ring. The scope of substrates includes para-substituted acetophenones for which selective HDO was observed with a beneficial effect of electron-donating substituents. Importantly, HDO activity was not observed with FeRu@SILP, CoRu@SILP, or CoRh@SILP bimetallic catalysts previously reported by our groups. Thus, the remarkably high HDO activity of $Fe_{40}Pt_{60}$@SILP, without acid addition, is presumably originating from synergetic interactions between Pt and Fe. These results show that a careful control of the Fe:Pt ratio in Fe_xPt_{100-x}@SILP materials allows the preparation of multifunctional catalytic systems with tailor-made reactivity toward challenging transformations involving H_2 activation and transfer.

SUPPORTING INFORMATION

Experimental details, materials and methods, and supplementary characterization data.

ACKNOWLEDGEMENTS

We thank Adeline Pham and Angélique Gillet for experimental support. We thank Alina Jakubowski, Annika Gurowski, Justus Werkmeister for GC and GC-MS measurements, Theresa Hungria, from the Castaing platform, for HR-TEM and STEM-EDX measurements, and Simon Cayez for help in SEM-EDX measurements. Financial supports from Agence Nationale de la Recherche (MOSC grant ANR-18-CE09-0007) is acknowledged. This work has been partially supported through the EUR grant NanoX n° ANR-

17-EURE-0009 in the framework of the Programme des Investissements d'Avenir. We acknowledge financial support by the Max Planck Society and by the Deutsche Forschungsgemeinschaft (DFG, German Research Foundation) under Germany's Excellence Strategy – Exzellenzcluster 2186 ''The Fuel Science Center'' ID: 390919832.

REFERENCES

(1) Voorhees, V.; Adams, R. The Use of the Oxides of Platinum for the Catalytic Reduction of Organic Compounds. I. *J. Am. Chem. Soc.* **1922**, *44* (6), 1397–1405. https://doi.org/10.1021/ja01427a021.

(2) Zelinsky, N. D.; Glinka, N. Uber Gleichseitige Reduktione- Und Oxydationekatalyse. *Berichte der Dtsch. Chem. Gesellschaft* **1911**, *44*, 2305–2312.

(3) Yan, G.; Feng, Y.; Long, S.; Zeng, X.; Sun, Y.; Tang, X.; Lin, L. Challenges with Biomass Waste Valorisation. In *Waste Valorisation: Waste Streams in a Circular Economy*; John Wiley & Sons, 2020; pp 183–202. https://doi.org/10.1002/9781119502753.ch8.

(4) Zaera, F. Designing Sites in Heterogeneous Catalysis: Are We Reaching Selectivities Competitive With Those of Homogeneous Catalysts? *Chem. Rev.* **2022**, *122* (9), 8594–8757. https://doi.org/10.1021/acs.chemrev.1c00905.

(5) Yu, W.; Porosoff, M. D.; Chen, J. G. Review of Pt-Based Bimetallic Catalysis: From Model Surfaces to Supported Catalysts. *Chem. Rev.* **2012**, *112* (11), 5780–5817. https://doi.org/10.1021/cr300096b.

(6) Luneau, M.; Lim, J. S.; Patel, D. A.; Sykes, E. C. H.; Friend, C. M.; Sautet, P. Guidelines to Achieving High Selectivity for the Hydrogenation of α,β-Unsaturated Aldehydes with Bimetallic and Dilute Alloy Catalysts: A Review. *Chem. Rev.* **2020**, *120* (23), 12834–12872. https://doi.org/10.1021/acs.chemrev.0c00582.

(7) Mustieles Marin, I.; Asensio, J. M.; Chaudret, B. Bimetallic Nanoparticles Associating Noble Metals and First-Row Transition Metals in Catalysis. *ACS Nano* **2021**, *15* (3), 3550–3556. https://doi.org/10.1021/acsnano.0c09744.

(8) Bordet, A.; Leitner, W. Metal Nanoparticles Immobilized on Molecularly Modified Surfaces: Versatile Catalytic Systems for Controlled Hydrogenation and Hydrogenolysis. *Acc. Chem. Res.* **2021**, 54, 2144-2157. https://doi.org/10.1021/acs.accounts.1c00013.

(9) Robinson, A. M.; Hensley, J. E.; Will Medlin, J. Bifunctional Catalysts for Upgrading of Biomass-Derived Oxygenates: A Review. *ACS Catal.* **2016**, *6* (8), 5026–5043. https://doi.org/10.1021/acscatal.6b00923.

(10) Román-Leshkov, Y.; Barrett, C. J.; Liu, Z. Y.; Dumesic, J. A. Production of Dimethylfuran for Liquid Fuels from Biomass-Derived Carbohydrates. *Nature* **2007**, *447* (7147), 982–985. https://doi.org/10.1038/nature05923.

(11) Furukawa, S.; Komatsu, T. Selective Hydrogenation of Functionalized Alkynes to (E)-Alkenes, Using Ordered Alloys as Catalysts. *ACS Catal.* **2016**, *6* (3), 2121–2125. https://doi.org/10.1021/acscatal.5b02953.

(12) Le, S. D.; Nishimura, S. Highly Selective Synthesis of 1,4-Butanediol via Hydrogenation of Succinic Acid with Supported Cu-Pd Alloy Nanoparticles. *ACS Sustain. Chem. Eng.* **2019**, *7* (22), 18483–18492. https://doi.org/10.1021/acssuschemeng.9b04447.

(13) Iihama, S.; Furukawa, S.; Komatsu, T. Efficient Catalytic System for Chemoselective Hydrogenation of Halonitrobenzene to Haloaniline Using PtZn Intermetallic Compound. *ACS Catal.* **2016**, *6* (2), 742–746. https://doi.org/10.1021/acscatal.5b02464.

(14) Mitsudome, T.; Miyagawa, K.; Maeno, Z.; Mizugaki, T.; Jitsukawa, K.; Yamasaki, J.; Kitagawa, Y.; Kaneda, K. Mild Hydrogenation of Amides to Amines over a Platinum-Vanadium Bimetallic Catalyst. *Angew. Chemie - Int. Ed.* **2017**, *56* (32), 9381–9385. https://doi.org/10.1002/anie.201704199.

(15) Nguyen, T. S.; Laurenti, D.; Afanasiev, P.; Konuspayeva, Z.; Piccolo, L. Titania-Supported Gold-Based Nanoparticles Efficiently Catalyze the Hydrodeoxygenation of Guaiacol. *J. Catal.* **2016**, *344*, 136–140. https://doi.org/10.1016/j.jcat.2016.09.016.

(16) Wang, X.; Arai, M.; Wu, Q.; Zhang, C.; Zhao, F. Hydrodeoxygenation of Lignin-Derived Phenolics-a Review on the Active Sites of Supported Metal Catalysts. *Green Chem.* **2020**, *22* (23), 8140–8168. https://doi.org/10.1039/d0gc02610g.

(17) Luo, J.; Yun, H.; Mironenko, A. V.; Goulas, K.; Lee, J. D.; Monai, M.; Wang, C.; Vorotnikov, V.; Murray, C. B.; Vlachos, D. G.; Fornasiero, P.; Gorte, R. J. Mechanisms for High Selectivity in the Hydrodeoxygenation of 5-Hydroxymethylfurfural over PtCo Nanocrystals. *ACS Catal.* **2016**, *6* (7), 4095–4104. https://doi.org/10.1021/acscatal.6b00750.

(18) Pino, N.; Sitthisa, S.; Tan, Q.; Souza, T.; López, D.; Resasco, D. E. Structure, Activity, and Selectivity of Bimetallic Pd-Fe/SiO2 and Pd-Fe/Γ-Al2O3 Catalysts for the Conversion of Furfural. *J. Catal.* **2017**, *350*, 30–40. https://doi.org/10.1016/j.jcat.2017.03.016.

(19) Liu, X.; Wang, C.; Zhang, Y.; Qiao, Y.; Pan, Y.; Ma, L. Selective Preparation of 4-Alkylphenol from Lignin-Derived Phenols and Raw Biomass over Magnetic Co–Fe@N-Doped Carbon Catalysts. *ChemSusChem* **2019**, *12* (21), 4791–4798. https://doi.org/10.1002/cssc.201901578.

(20) Bordet, A.; Leitner, W. Metal Nanoparticles Immobilized on Molecularly Modified Surfaces: Versatile Catalytic Systems for Controlled Hydrogenation and Hydrogenolysis. *Acc. Chem. Res.* **2021**, *54* (9), 2144–2157. https://doi.org/10.1021/acs.accounts.1c00013.

(21) Luska, K. L.; Bordet, A.; Tricard, S.; Sinev, I.; Grünert, W.; Chaudret, B.; Leitner, W. Enhancing the Catalytic Properties of Ruthenium Nanoparticle-SILP Catalysts by Dilution with Iron. *ACS Catal.* **2016**, *6* (6), 3719–3726. https://doi.org/10.1021/acscatal.6b00796.

(22) Sisodiya-Amrute, S.; Van Stappen, C.; Rengshausen, S.; Han, C.; Sodreau, A.; Weidenthaler, C.; Tricard, S.; DeBeer, S.; Chaudret, B.; Bordet, A.; Leitner, W. Bimetallic MxRu100−x Nanoparticles (M = Fe, Co) on Supported Ionic Liquid Phases (MxRu100−x@SILP) as Hydrogenation Catalysts: Influence of M and M:Ru Ratio on Activity and Selectivity. *J. Catal.* **2022**, *407*, 141–148. https://doi.org/10.1016/j.jcat.2022.01.030.

(23) Rengshausen, S.; Van Stappen, C.; Levin, N.; Tricard, S.; Luska, K. L.; DeBeer, S.; Chaudret, B.; Bordet, A.; Leitner, W. Organometallic Synthesis of Bimetallic Cobalt-Rhodium Nanoparticles in Supported Ionic Liquid Phases (CoxRh100−x@SILP) as Catalysts for the Selective Hydrogenation of Multifunctional Aromatic Substrates. *Small* **2021**, *17* (5), 1–10. https://doi.org/10.1002/smll.202006683.

(24) Serantes, D.; Spasova, M.; Baldomir, D.; Farle, M.; Salgueirino, V. Magnetic Hardness of Fe60Pt40 Nanoparticles Controlled by Surface Chemistry. *Chem. Mater.* **2010**, *22* (13), 4103–4110. https://doi.org/10.1021/cm1010967.

(25) Pousthomis, M.; Garnero, C.; Marcelot, C. G.; Blon, T.; Cayez, S.; Cassignol, C.; Du, V. A.; Krispin, M.; Arenal, R.; Soulantica, K.; Viau, G.; Lacroix, L. M. On the Advantages of Spring Magnets Compared to Pure FePt: Strategy for Rare-Earth Free Permanent Magnets Following a Bottom-up Approach. *J. Magn. Magn. Mater.* **2017**, *424* (September 2016), 304–313. https://doi.org/10.1016/j.jmmm.2016.10.071.

(26) Sun, S.; Murray, C. B.; Weller, D.; Folks, L.; Moser, A. MonodSun, S., Murray, C. B., Weller, D., Folks, L., & Moser, A. (2000). Monodisperse FePt Nanoparticles and Ferromagnetic FePt Nanocrystal Superlattices. Science, 287(5460), 1989–1992. Https://Doi.Org/10.1126/Science.287.5460.1989isperse FePt Nanoparticle. *Science (80-.).* **2000**, *287* (5460), 1989–1992.

(27) Liu, Z.; Tan, X.; Li, J.; Lv, C. Easy Synthesis of Bimetal PtFe-Containing Ordered Mesoporous Carbons and Their Use as Catalysts for Selective Cinnamaldehyde Hydrogenation. *New J. Chem.* **2013**, *37* (5), 1350–1357. https://doi.org/10.1039/c3nj40946e.

(28) Zhang, W.; Xin, H.; Zhang, Y.; Jin, X.; Wu, P.; Xie, W.; Li, X. Bimetallic Pt-Fe Catalysts Supported on Mesoporous TS-1 Microspheres for the Liquid-Phase Selective Hydrogenation of Cinnamaldehyde. *J. Catal.* **2021**, *395*, 375–386. https://doi.org/10.1016/j.jcat.2021.01.034.

(29) Neri, G.; Arrigo, I.; Corigliano, F.; De Luca, L.; Donato, A. Selective Hydrogenation of Cinnamaldehyde on Pt and Pt-Fe Catalysts Supported on Zeolite P. *Catal. Letters* **2011**, *141* (11), 1590–1597. https://doi.org/10.1007/s10562-011-0688-x.

(30) Bai, S.; Bu, L.; Shao, Q.; Zhu, X.; Huang, X. Multicomponent Pt-Based Zigzag Nanowires as Selectivity Controllers for Selective Hydrogenation Reactions. *J. Am. Chem. Soc.* **2018**, *140* (27), 8384–8387. https://doi.org/10.1021/jacs.8b03862.

(31) Guo, S.; Li, D.; Zhu, H.; Zhang, S.; Markovic, N. M.; Stamenkovic, V. R.; Sun, S. FePt and CoPt Nanowires as Efficient Catalysts for the Oxygen Reduction Reaction. *Angew. Chemie - Int. Ed.* **2013**, *52* (12), 3465–3468. https://doi.org/10.1002/anie.201209871.

(32) Zeng, S.; Lv, B.; Qiao, J.; Yang, W.; Zhu, C.; Zhang, Y.; Hu, D.; Chen, M.; Di, J.; Li, Q. PtFe Alloy Nanoparticles Confined on Carbon Nanotube Networks as Air Cathodes for Flexible and Wearable Energy Devices. *ACS Appl. Nano Mater.* **2019**, *2* (12), 7870–7879. https://doi.org/10.1021/acsanm.9b01865.

(33) Crabb, E. M.; Marshall, R. Properties of Alumina Supported Pd-Fe and Pt-Fe Catalysts Prepared Using Surface Organometallic Chemistry. *Appl. Catal. A Gen.* **2001**, *217* (1–2), 41–53. https://doi.org/10.1016/S0926-860X(01)00578-6.

(34) Geng, Y.; Chen, C.; Gao, Z.; Feng, X.; Liu, W.; Li, Y.; Jin, T.; Shi, Y.; Zhang, W.; Bao, M. Unsupported Nanoporous Platinum-Iron Bimetallic Catalyst for the Chemoselective Hydrogenation of Halonitrobenzenes to Haloanilines. *ACS Appl. Mater. Interfaces* **2021**, *13* (20), 23655–23661. https://doi.org/10.1021/acsami.1c02734.

(35) Mori, K.; Yoshioka, N.; Kondo, Y.; Takeuchi, T.; Yamashita, H. Catalytically Active, Magnetically Separable, and Water-Soluble FePt Nanoparticles Modified with Cyclodextrin for Aqueous Hydrogenation Reactions. *Green Chem.* **2009**, *11* (9), 1337–1342. https://doi.org/10.1039/b905331j.

(36) Siani, A.; Alexeev, O. S.; Lafaye, G.; Amiridis, M. D. The Effect of Fe on SiO2-Supported Pt Catalysts: Structure, Chemisorptive, and Catalytic Properties. *J. Catal.* **2009**, *266* (1), 26–38. https://doi.org/10.1016/j.jcat.2009.05.013.

(37) Jiang, Z.; Wan, W.; Lin, Z.; Xie, J.; Chen, J. G. Understanding the Role of M/Pt(111) (M = Fe, Co, Ni, Cu) Bimetallic Surfaces for Selective Hydrodeoxygenation of Furfural. *ACS Catal.* **2017**, *7* (9), 5758–5765. https://doi.org/10.1021/acscatal.7b01682.

(38) Thallada, B.; Kumar, A.; Jindal, M.; Maharana, S. Lignin Biorefinery: New Horizons in Catalytic Hydrodeoxygenation for the Production of Chemicals. *Energy and Fuels* **2021**, *35* (21), 16965–16994. https://doi.org/10.1021/acs.energyfuels.1c01651.

(39) Bordet, A.; Moos, G.; Welsh, C.; Licence, P.; Luska, K. L.; Leitner, W. Molecular Control of the Catalytic Properties of Rhodium Nanoparticles in Supported Ionic Liquid Phase (SILP) Systems. *ACS Catal.* **2020**, *10* (23), 13904–13912. https://doi.org/10.1021/acscatal.0c03559.

(40) Goclik, L.; Walschus, H.; Bordet, A.; Leitner, W. Selective Hydrodeoxygenation of Acetophenone Derivatives Using a Fe 25 Ru 75 @SILP Catalyst: A Practical Approach to the Synthesis of Alkyl Phenols and Anilines . *Green Chem.* **2022**, *24* (7), 2937–2945. https://doi.org/10.1039/d1gc04189d.

(41) Aleksandrov, H. A.; Neyman, K. M.; Hadjiivanov, K. I.; Vayssilov, G. N. Can the State of Platinum Species Be Unambiguously

Determined by the Stretching Frequency of an Adsorbed CO Probe Molecule? *Phys. Chem. Chem. Phys.* **2016**, *18* (32), 22108–22121. https://doi.org/10.1039/c6cp03988j.

(42) Meunier, F.; Kdhir, R.; Potrzebowska, N.; Perret, N.; Meunier, F.; Kdhir, R.; Potrzebowska, N.; Perret, N.; Unravelling, M. B. Unravelling Platinum-Zirconia Interfacial Sites Using CO Adsorption . **2021**, 0–24.

(43) Seenivasan, K.; Gallo, E.; Piovano, A.; Vitillo, J. G.; Sommazzi, A.; Bordiga, S.; Lamberti, C.; Glatzel, P.; Groppo, E. Silica-Supported Ti Chloride Tetrahydrofuranates, Precursors of Ziegler-Natta Catalysts. *Dalt. Trans.* **2013**, *42* (35), 12706–12713. https://doi.org/10.1039/c3dt50603g.

(44) Siani, A.; Alexeev, O. S.; Captain, B.; Lafaye, G.; Marécot, P.; Adams, R. D.; Amiridis, M. D. Synthesis of Cluster-Derived PtFe/SiO2 Catalysts for the Oxidation of CO. *J. Catal.* **2008**, *255* (2), 162–179. https://doi.org/10.1016/j.jcat.2008.01.031.

(45) Gong, X.; Shi, Q.; Zhang, X.; Li, J.; Ping, G.; Xu, H.; Ding, H.; Li, G. Synergistic Effects of PtFe/CeO2 Catalysts Afford High Catalytic Performance in Selective Hydrogenation of Cinnamaldehyde. *J. Rare Earths* **2023**, *41* (2), 233–239. https://doi.org/10.1016/j.jre.2022.02.010.

(46) Respaud, M.; Broto, J.; Rakoto, H.; Fert, A. R.; Thomas, L.; Barbara, B.; Verelst, M.; Snoeck, E.; Lecante, P.; Mosset, A.; Osuna, J.; Ould Ely, T.; Amiens, C.; Chaudret, B. Surface Effects on the Magnetic Properties of Ultrafine Cobalt Particles. *Phys. Rev. B - Condens. Matter Mater. Phys.* **1998**, *57* (5), 2925–2935. https://doi.org/10.1103/PhysRevB.57.2925.

(47) Michael, C.; Stuart, P. S. P. *Handbook of Magnetism and Magnetic Materials*; Springer, 2021.

(48) Surburg, H.; Panten, J. *Common Fragrance and Flavor Materials*; VCH Weinheim, 2006. https://doi.org/10.1002/3527608214.

(49) Weissermel, K.; Arpe, H.-J. *Industrial Organic Chemistry*, 3rd ed.; VCH Weinheim, 1997.

(50) Kim, S.; Kwon, E. E.; Kim, Y. T.; Jung, S.; Kim, H. J.; Huber, G. W.; Lee, J. Recent Advances in Hydrodeoxygenation of Biomass-Derived Oxygenates over Heterogeneous Catalysts. *Green Chem.* **2019**, *21* (14), 3715–3743. https://doi.org/10.1039/c9gc01210a.

(51) Jing, Y.; Dong, L.; Guo, Y.; Liu, X.; Wang, Y. Chemicals from Lignin: A Review of Catalytic Conversion Involving Hydrogen. *ChemSusChem* **2020**, *13* (17), 4181–4198. https://doi.org/10.1002/cssc.201903174.

(52) Zhang, J.; Ellis, L. D.; Wang, B.; Dzara, M. J.; Sievers, C.; Pylypenko, S.; Nikolla, E.; Medlin, J. W. Control of Interfacial Acid-Metal Catalysis with Organic Monolayers. *Nat. Catal.* **2018**, *1* (2), 148–155. https://doi.org/10.1038/s41929-017-0019-8.

(53) Offner-Marko, L.; Bordet, A.; Moos, G.; Tricard, S.; Rengshausen, S.; Chaudret, B.; Luska, K. L.; Leitner, W. Bimetallic Nanoparticles in Supported Ionic Liquid Phases as Multifunctional Catalysts for the Selective Hydrodeoxygenation of Aromatic Substrates. *Angew. Chemie - Int. Ed.* **2018**, *57* (39), 12721–12726. https://doi.org/10.1002/anie.201806638.

(54) Morin, C.; Simon, D.; Sautet, P. Intermediates in the Hydrogenation of Benzene to Cyclohexene on Pt(1 1 1) and Pd(1 1 1): A Comparison from DFT Calculations. *Surf. Sci.* **2006**, *600* (6), 1339–1350. https://doi.org/10.1016/j.susc.2006.01.033.

(55) Zong, R.; Li, H.; Ding, W. T.; Huang, H. Highly Dispersed Pd on Zeolite/Carbon Nanocomposites for Selective Hydrodeoxygenation of Biomass-Derived Molecules under Mild Conditions. *ACS Sustain. Chem. Eng.* **2021**, *9* (29), 9891–9902. https://doi.org/10.1021/acssuschemeng.1c02876.

(56) Wang, J.; Zhang, Y.; Zhang, M.; Wang, Z.; Zhang, M. Hydrodeoxygenation of Acetophenone over a Sulfonated Carbon-Supported Ruthenium Catalyst. *Catal. Today* **2018**, *314*, 164–169. https://doi.org/10.1016/j.cattod.2017.11.034.

(57) Li, H.; Li, H.; Gao, Z.; Gao, Z.; Lei, L.; Liu, H.; Han, J.; Han, J.; Hong, F.; Hong, F.; Luo, N.; Wang, F. Photocatalytic Transfer Hydrogenolysis of Aromatic Ketones Using Alcohols. *Green Chem.* **2020**, *22* (12), 3802–3808. https://doi.org/10.1039/d0gc00732c.

(58) Han, S.; Gao, R.; Sun, M. S.; Zhou, Y.; Chen, W. T.; Liu, X.; Qin, J.; Tao, D. J.; Zhang, Z. Synergistic Roles of Single Co Atoms and Co Nanoparticles for the Hydrodeoxygenation and Ring Hydrogenation Reactions. *J. Phys. Chem. C* **2023**, 127, 14185-14196. https://doi.org/10.1021/acs.jpcc.3c02352.

(59) Ning, H.; Chen, Y.; Wang, Z.; Mao, S.; Chen, Z.; Gong, Y.; Wang, Y. Selective Upgrading of Biomass-Derived Benzylic Ketones by (Formic Acid)–Pd/HPC–NH2 System with High Efficiency under Ambient Conditions. *Chem* **2021**, *7* (11), 3069–3084. https://doi.org/10.1016/j.chempr.2021.07.002.

(60) Goclik, L.; Offner-Marko, L.; Bordet, A.; Leitner, W. Selective Hydrodeoxygenation of Hydroxyacetophenones to Ethyl-Substituted Phenol Derivatives Using a FeRu@SILP Catalyst. *Chem. Commun.* **2020**, *56* (66), 9509–9512. https://doi.org/doi.org/10.1039/D0CC03695A.

(61) Asensio, J. M.; Miguel, A. B.; Fazzini, P. F.; van Leeuwen, P. W. N. M.; Chaudret, B. Hydrodeoxygenation Using Magnetic Induction: High-Temperature Heterogeneous Catalysis in Solution. *Angew. Chemie - Int. Ed.* **2019**, *58* (33), 11306–11310. https://doi.org/10.1002/anie.201904366.

(62) Stassi, J. P.; Zgolicz, P. D.; De Miguel, S. R.; Scelza, O. A. Formation of Different Promoted Metallic Phases in PtFe and PtSn Catalysts Supported on Carbonaceous Materials Used for Selective Hydrogenation. *J. Catal.* **2013**, *306*, 11–29. https://doi.org/10.1016/j.jcat.2013.05.029.

(63) Wang, Y.; Qin, R.; Wang, Y.; Ren, J.; Zhou, W.; Li, L.; Ming, J.; Zhang, W.; Fu, G.; Zheng, N. Chemoselective Hydrogenation of

Nitroaromatics at the Nanoscale Iron(III)–OH–Platinum Interface. *Angew. Chemie - Int. Ed.* **2020**, *59* (31), 12736–12740. https://doi.org/10.1002/anie.202003651.

(64) Luo, J.; Lee, J. D.; Yun, H.; Wang, C.; Monai, M.; Murray, C. B.; Fornasiero, P.; Gorte, R. J. Base Metal-Pt Alloys: A General Route to High Selectivity and Stability in the Production of Biofuels from HMF. *Appl. Catal. B Environ.* **2016**, *199*, 439–446. https://doi.org/10.1016/j.apcatb.2016.06.051.